# *Chapter 5*

# Simulator validation

Following on from the two previous chapters, which considered the model of the simulation process and how this model was implemented in software, this chapter is concerned with validation of the software.

## 5.1 Introduction

Validation can be performed in many different ways (see Figure 5.1). The ideal validation will have three characteristics. Firstly, it will be quantitative. Secondly, it will use a realistic object, a brain. Thirdly, it will use real scanning data for the comparison with the simulated data. However, it is not often possible to have all these three characteristics present in one validation process. This is because of the large number of scanning factors inherent in the brain scanning process (for example motion, $B_0$ inhomogeneity, their interactions or BOLD etc.). It is difficult to isolate these factors from one another and therefore to use them in a quantitative validation process. Because of this reason, the approach taken in this thesis has been to use a series of non-ideal types of validations using simpler objects or simple theoretical models (which were experimentally validated in the past), or having purely qualitative results (the simulated images are compared to the experimental images visually). The series of these, although not completely ideal validations, are still quite significant and should be sufficient for the reliable use of the simulator.

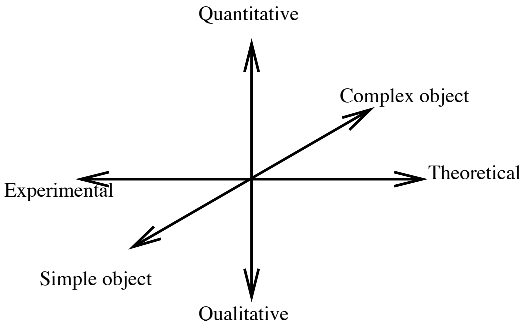

Figure 5.1: A descriptive representation of the different ways a validation can be performed. The x-axis represents whether experimental data or simple theoretical models (experimentally validated in the past) were used for the comparison with the simulated signal. The z-axis describes whether this comparison was done quantitatively or qualitatively. The y-axis describes the input object used. Complexity of the object describes how realistic object is. For example, the brain is the most realistic object. A simple geometrically shaped object (e.g. a sphere) with only one tissue type is an example of a simple object.

Each module of the simulator is validated through a series of independent process which are set out in this chapter. An investigation regarding the properties of the input object is done. More specifically, the sensitivity of the simulator regarding the object voxel size is investigated. This is done by comparing the simulated results for various voxel sizes against the analytically calculated results as if the object is continuous.

The magnetic-susceptibility-induced $B_0$ inhomogeneity model is validated indirectly using known theoretical models which were experimentally validated by other research groups (more details including the references are set out in the section). Some qualitative results are set out as well. The effect of the $B_0$ inhomogeneities was also validated through an application in neuronal current imaging which is set out in Chapter 6, Section 6.

The motion model is validated experimentally. The main focus was on the translation in the z direction, where the effects of spin-history were looked at, and the rotation about the y-axis, where the interaction of the motion and the $B_0$ inhomogeneities was looked at. In addition to this, a purely qualitative result showing blurring due to the rotation about the z-axis is shown. The motion model was also validated through a few applications which are set out in Chapter 6, Sections 2-4.

The chemical shift model is validated indirectly using known theoretical models. Results were generated for a realistic brain phantom and the chemical shift measure was taken for the fat tissue that was part of the brain phantom.

Implementation of the BOLD model and eddy currents model are validated through applications shown in Chapter 6, Sections 4 and 5 respectively. The validation of the physiological basis of the BOLD model was not done as it is beyond the scope of this thesis. The use of the $T_2^*$ changes in order to simulate the BOLD signal in the simulator was based on the works published by Ogawa et al. [57], [58].

The material just described is organised into three groups and presented as three different sections in this chapter. Firstly the results for quantitative comparison of the simulator output with theoretical results are presented. Following this, results for quantitative comparison of the simulator output with the real scanning images are presented. Lastly, qualitative results which demonstrate the possibility of simulation of images impacted by realistic artefacts are presented.

## 5.2 Quantitative comparison of the simulator output with the theoretical results

In this section we compare the output of the simulations with the theoretical models which are well known and are well established and used in the MRI community. We start with the evaluation of the simulator with respect to the size of the object voxels, then we validate simulator contrast generation and finally we validate simulation of the simple $B_0$ inhomogeneity effects for which the theoretical results are well documented.

### 5.2.1 Evaluation of the simulator performance for different object voxel sizes

Input objects for the simulator are discrete, voxel-based volumes and the accurate representation of the underlying structure (virtual brain) depends on the object voxel size, which then influences the simulator output. In order to investigate the sensitivity of the simulator to object voxel size, we have compared images simulated for the discrete objects with varying voxel sizes, with the one generated analytically for a truly continuous object. This was done separately for the in-plane object voxel size ($x$- and $y$- direction) and for the through-slice object voxel size ($z$- direction) as the two have a different impact on the signal.

#### In-plane tests

For the in-plane tests we have chosen an ellipsoid as an input object with dimensions such that it resembles a normal human brain. In order to be able to calculate an analytical solution the area inside the ellipsoid is homogeneous (with spin density equal to one) and the MRI parameters were chosen in order to obtain a simulated k-space with no $T_2^*$ decay ($T_2^* = 100$ s). One 1mm slice was simulated and simulations were done for a series of object voxel sizes ranging from $5.5 \times 5.5$mm to $0.1 \times 0.1$mm in plane. An analytic k-space $S$ was calculated by using the analytical expression for the Fourier transform of the ellipse, and evaluating it at the k-space points $(k_x, k_y)$ generated by the same pulse sequence as the one used in simulations:

$$\begin{aligned} S(k_x, k_y) &= (\frac{ab}{C} J_1(2\pi C) \cos(2\pi(k_x x_0 + k_y y_0)), \frac{ab}{C} J_1(2\pi C) \sin(2\pi(k_x x_0 + k_y y_0))) \\ C &= \sqrt{(ak_x \cos(\theta) + ak_y \sin(\theta))^2 + (bk_y \cos(\theta) - bk_x \sin(\theta))^2} \qquad (5.1) \end{aligned}$$

where $a, b$ are the semimajor and semiminor axes of the ellipse, $x_0, y_0$ is the center of the ellipse and $\theta$ is the angle between its major axis and the x-axis and $J_1$ is the Bessel's function of the first order.

In order to evaluate the error of the simulated k-spaces (compared to the analytical k-space) the Root Mean Square (RMS) value was calculated for the difference between analytically calculated k-space $S_a(k_x, k_y)$ and each of the simulated k-spaces $S(k_x, k_y)$. This value was divided with the RMS value of the analytically calculated k-space and in addition multiplied with 100, giving the accuracy as a percentage of the analytically calculated k-space (Figure 5.2):

$$Error = 100 \frac{\sqrt{\frac{1}{4096} \sum_{k_x, k_y = 1}^{64} (S_a(k_x, k_y) - S(k_x, k_y))^2)}}{\sqrt{\frac{1}{4096} \sum_{k_x, k_y = 1}^{64} (S_a(k_x, k_y))^2)}}. \qquad (5.2)$$

The results show that the error in the simulated signal is less than 0.5% of the analytical solution for object voxel sizes that are smaller than $1 \times 1$mm in-plane. This is likely to be an acceptable error for FMRI sequences, since typical noise levels are around 1-2% of the total signal mean. With the decrease in object voxel size, the computational time for the simulation increases, which is shown with the red line in Figure 5.2. In order to spend the least amount of computational time but also not compromise the simulated data, we choose the object voxel

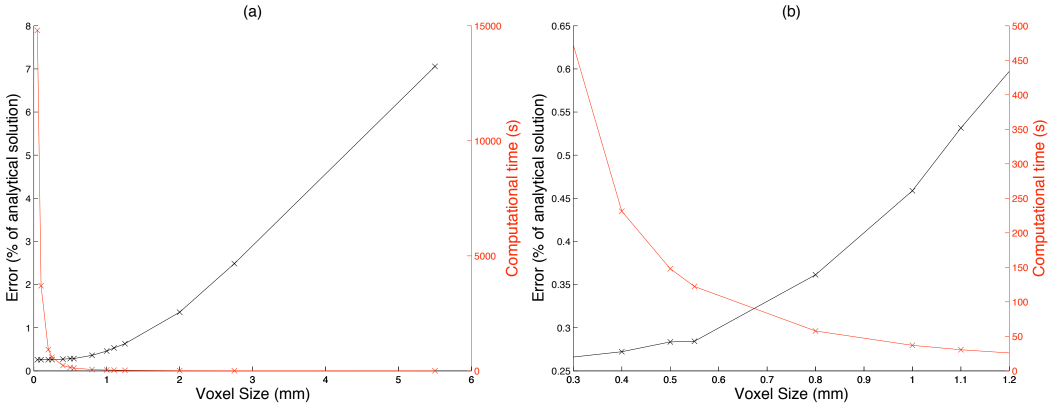

Figure 5.2: The black line and black $y$-axis in both of the plots show the RMS-based difference between the analytically calculated k-space and simulated k-spaces expressed as a percentage of the analytically calculated k-space signal (plot (b) is an enlarged inset of plot (a)). The red line and the red $y$-axis show the computational time which it took for the generation of the simulations. It can be seen from the plot (b) that for voxel sizes which are less than $1 \times 1$mm in plane, the error in the simulations is less than 0.5% which is likely to be an acceptable error for FMRI sequences, since typical noise levels are around 1-2% of the total signal mean. However, the computational time is increasing as the voxel size goes down, therefore the optimal voxel size depends on the specific simulation and whether the accuracy or the computational speed is a priority.

size according to the simulations we are running, which is $1 \times 1$mm in plane for most applications. When decreasing the object voxel size $n$ times for each in-plane dimension, the computational time increases $n^2$ times. For example, for a typical FMRI sequence described in Section 4.5.3, and for an object voxel of $0.5 \times 0.5$mm in plane, the error decreases to 0.2%. However, the computational time increases by 400% (from 42h30m to 170h) which would often be prohibitive for one processor and makes an additional 0.2% error an acceptable tradeoff.

### Through-slice tests

For the through-slice tests we have chosen to do tests with a simple homogeneous cubic object (with spin density equal to one) for which we can derive an analytical solution. The main sensitivity of the signal with respect to the object voxel size in the through-slice direction is due to the excitation mechanism. The excitation of an object voxel is determined by the frequency value at its center. If the center of an object voxel is excited with a flip angle $\alpha$, the whole object voxel gets excited with that same flip angle, creating a piecewise-constant-shaped approximation of the given slice profile. In order to investigate the situation which will create the largest error, the case when the object is moving in the through-slice direction is investigated.

Parameters used for the simulations are: EPI pulse sequences with flip angles of 30°/60°/90°; square/windowed-sinc slice profiles); in-plane matrix $64 \times 64$; 1mm slice thickness; 3 sequential slices per volume; TR of 1.15s; $T_1 = 1.9$s, $T_2^* = 0.3$s and $\rho = 1$. Motion sequence consisted of two back and forth motions: the 20th volume was displaced by +3mm and the 30th volume was displaced by -1mm in the $z$-direction. The values for the experiment were taken from the paper by Muresan et.al. [55]. The object's total length in the $z$-direction was fixed and simulations were done for various object voxel sizes ranging from 1mm to 0.001mm in the $z$-direction.

Motion in the through-slice direction creates changes in the signal due to spin history effects. In a similar fashion as Muresan et.al. [55] these changes are represented using the relative intensity $\triangle I_t = 100\frac{I_t - I_{18}}{I_{18}}, t = (1, 2, ..40)$ of an image voxel situated in the middle slice. By the 18th volume the signal has reached its steady state and therefore the 18th volume is chosen as a reference volume. The results are shown in Figure 5.3 (a) and (b). The signal changes in the first few volumes are due to saturation effects, which in a case of 90° flip angle and an 'ideal' square slice profile is reached in one TR (all the simulations were done with perfectly homogeneous RF and $B_0$ fields). Spin history effects can be seen in the areas of the 20th and 30th volume. For an 'ideal' square slice profile the steady state was re-established much quicker than for the windowed-sinc slice profile confirming the more complex situation when a variety of object voxels with different flip angles are present.

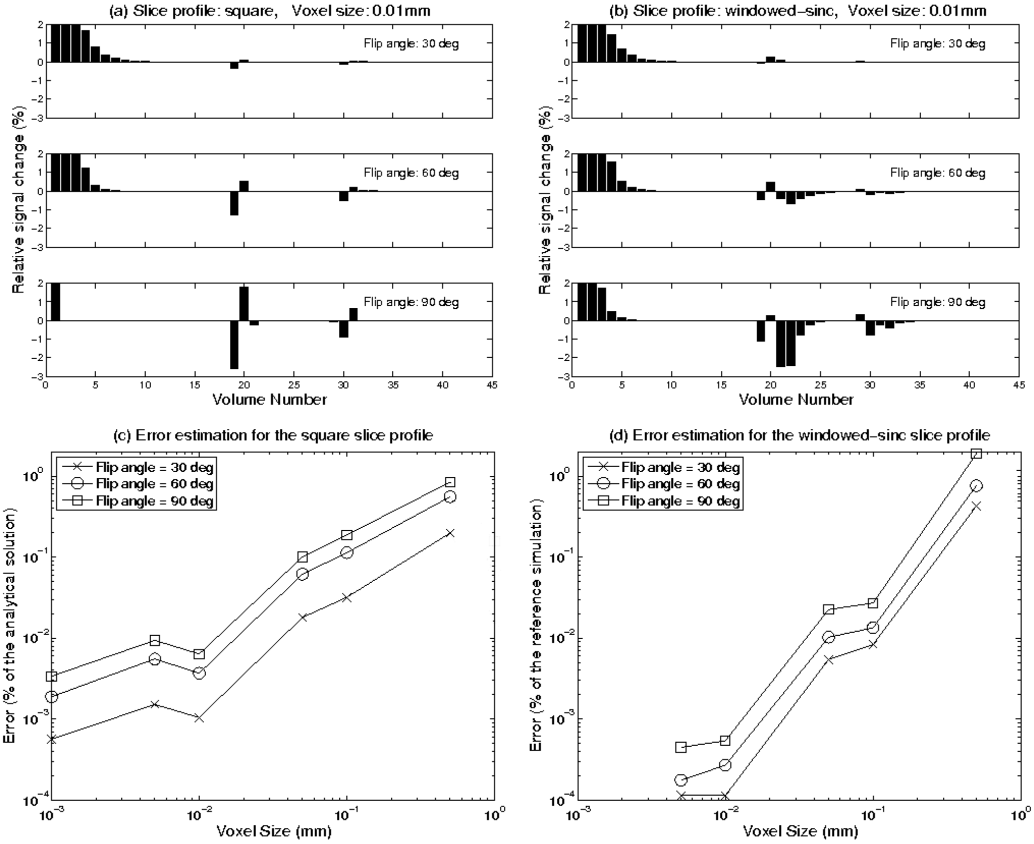

Figure 5.3: (a) and (b) show relative change in the simulated signal due to saturation effects (first few volumes) and the spin history effects caused by the motion in through-slice direction (areas of 20th and 30th volume in the sequence). Different extents to which the spin history influences the signal for different slice profiles can be seen when comparing plots (a), generated with an 'ideal' square slice profile, and (b), generated with a realistic windowed-sinc slice profile. Simulations in (a) and (b) were done with a 0.01mm object voxel size which is generated with a mean error of less than (a) 0.01% of the analytical solution; (b) 0.001% of the simulation for an object voxel size of 0.001mm (we refer to it in plots as the 'reference simulation'). Mean error for various other voxel sizes in range from 0.001mm to 1mm was calculated and is represented in the plots (c) and (d).

The accuracy of the simulations was tested separately for the case of an 'ideal' square slice profile and the case of the realistic windowed-sinc slice profile. For an 'ideal' square slice profile a solution based on theory was calculated using Eq. [3.3] and Eq. [3.5]. This solution was compared against simulations generated with different object voxel sizes using equation $error(v) = \mathrm{mean}_t(|\triangle I_t(v) - \triangle A_t|), t = (1, 2, ..40)$ where $v$ is the object voxel size, $\triangle I_t$ is the relative signal intensity of the simulations and $\triangle A_t$ is the relative signal intensity of the analytical solution at the time point $t$ (intensities are in k-space).

The results can be seen in Figure 5.3 (c). They show that in order to obtain a reasonable and acceptable simulation accuracy for an 'ideal' square slice profile (given noise levels of 1-2%), an object voxel size in through-slice direction needs to be 1mm or below. Error calculations for the windowed-sinc slice profile were calculated in the same way as for an 'ideal' square slice profile case, with the difference that instead of the analytical solution, simulation with an object voxel size 0.001mm was used as the reference. These results are shown in Figure 5.3 (d). For this situation, in order to achive acceptable errors of less than 1% of the reference signal, the object voxel size also needs to be 1mm or less. Note that all of the the simulations were done for the slice thickness of 1mm which is the worst possible case for the error estimation. In a realistic FMRI sequence slice thickness is usually 4mm or more, which considerably reduces the size of the error.

### 5.2.2 Image contrast

In order to test the simulation of image contrast in the software, the simulations were compared with the results derived from theoretical expressions for image contrast. These expressions can be found in Sections 15.4.3 and 15.4.4 of Haacke et.al. [29], where they are also plotted for $TE = 0$s (Figure 15.7) and long (infinite) $TR$ (Figure 15.8). These plots were recreated using the same theoretical expressions and parameters as in Haacke et.al., and are shown in Figure 5.4 (dashed lines). In the same figure, plots that use the same theoretical expressions

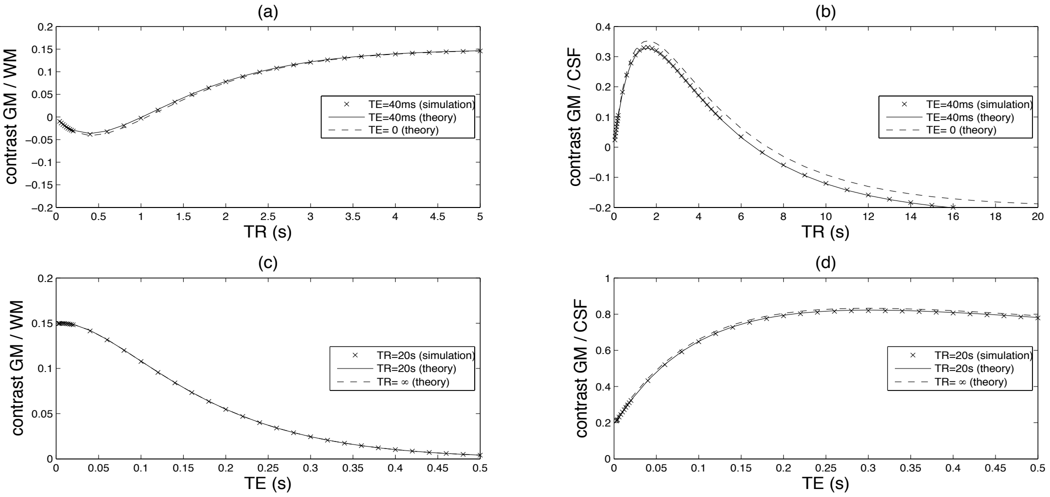

Figure 5.4: Figure shows contrast for (a), (c) gray matter and white matter; (b), (d) gray matter and CSF obtained for a 90° flip angle gradient echo experiment. Contrasts in (a) and (b) are shown as a function of TR for a $T_1$-weighted scan simulation with $TE = 40$ ms. Contrasts in (c) and (d) are shown as a function of TE for a $T_2^*$-weighted scan simulation with $TR = 20$ s. Simulation results are marked with crosses and they agree very well with the results derived from the theory (solid and dashed lines - described in the text).

and tissue parameters but more realistic sequence parameters, $TE = 40$ms and $TR = 20$s, are also shown (solid lines). Simulation results were generated using the latter, realistic values for $TE$ and $TR$ and are marked as crosses. From Figure 5.4 it can be seen that the simulation results agree very well with the theoretical results, implying the accuracy of the software implementation. These simple contrast models have been extensively tested in practice [29], [46]

### 5.2.3 $B_0$ inhomogeneities

In order to test the simulation of the $B_0$ inhomogeneity in the software, we independently investigate two main effects of the $B_0$ inhomogeneity in gradient-echo EPI: translation in the phase encode direction, and signal loss.

Input objects and the perturbed field were chosen such that the theoretical solution can be calculated. The input object was an ellipsoid (described at the beginning of this section), with the area inside the ellipsoid homogeneous (with spin density equal to one) and MRI parameters chosen in order to obtain a simulated k-space with minimal $T_2^*$ decay ($T_2^* = 100$ s). A perturbed $B_0$ field was chosen to be spatially constant for the case of testing the translation in the phase encode direction. However, for measuring the signal loss it was chosen to vary linearly, in the positive $z$ direction (through-slice). In this way, we were able to use theoretical results in order to calculate the expected amount of translation and signal loss and compare them to the simulation results.

Simulation results were generated for one 1mm thick slice, and an EPI pulse sequence with an 'ideal' square slice profile and flip angle of 90°. Theoretical results for the amount of translation and the signal loss were obtained by using Eqs. [5.3] which are derived in the same way as in Jezzard et.al. [38] and Deichmann et.al. [20]:

$$\begin{aligned} T_{PE} &= \frac{\gamma}{2\pi} B_p N_y \triangle y \left( \sqrt{\frac{8\ \tau\ \pi}{\gamma\ G_{max}\ N_y \triangle y}} + \frac{N_x - 1}{BW} \right) \\ \frac{\triangle S}{S} &= 1 - \mid \mathrm{sinc}\left(\frac{\gamma}{2\pi} \triangle z\ \frac{\mathrm{d}B_p}{\mathrm{d}z}\ TE\right) \mid \end{aligned} \tag{5.3}$$

where $T_{PE}$ is the amount of expected translation for each image voxel in phase encode direction, $B_p$ is the strength of the perturbed magnetic field, BW is the bandwidth, $(N_x, N_y)$ is the size of the k-space matrix, $\triangle y$ is the size of the image voxel in the phase encode direction, $\tau$ is the rise time of the gradient coils and $G_{max}$ is the maximum strength of the gradient coils. In the equation for the signal loss, $S$ is the 'ideal' signal, i.e. not affected with $B_0$ inhomogeneities, $\triangle S$ is the expected loss of the signal $S$ due to $B_0$ inhomogeneities, $\triangle z$ is the slice thickness, TE is the echo time. In order to obtain the distorted images, an analytic k-space was calculated by using the analytical expression for the Fourier transform of the ellipse (see Eq.[5.1]) and taking into account the theoretically calculated values for expected translation and signal loss (see Eq.[5.3]). Signal was evaluated using this analytical expression at the k-space points generated by the pulse sequence used in the simulations.

In order to show the amount of translation in the images affected with the offset in $B_0$ field, 1D profiles of the simulated 2D images are plotted in Figure 5.5 (a), (b) and compared with the 1D profile in a magnetic field with no field offset. Simulations were done for different pulse sequence parameters and perturbed field strengths. Two plots on the left hand side of the figure represent 1D image profiles for two different bandwidths $BW = 85KHz$ (a) and $BW = 100KHz$ (b), and three different values of constant perturbed $B_0$ field, $B_p = 0T$ (green line), $B_p = 1.5\mu T$ (black line), $B_p = 3\mu T$ (blue line). It can be seen in the plots that the amount of translation (which can be seen as a difference between the green line and the line in question) increases with the strength of the perturbed $B_p$ field. The analytically calculated translations for all of the simulated cases are: 1) $BW = 85KHz$, $B_p = 1.5\mu T$: 0.0127m (3.18 image voxels); 2) $BW = 85KHz$, $B_p = 3\mu T$: 0.0254m (6.36 image voxels); 3) $BW = 100KHz$, $B_p = 1.5\mu T$: 0.0109m (2.73 image voxels); 4) $BW = 100KHz$, $B_p = 3\mu T$: 0.0218m (5.46 image voxels). As expected, the higher bandwidth induced a smaller amount of translation than the lower bandwidth, which is due to the reduced k-space acquisition time. The dashed lines are the 1D image profiles of the analytic results and they agree very closely with the simulation results (often the difference can not be seen).

The plots also show Gibbs ringing effects due to the finiteness of the Fourier series in the process of image reconstruction (this can be more clearly seen in plot (c) which is an enlarged inset of plot (a)). The level of ringing changes as the object shifts: blue line - 0mm shift (0 image voxels); black line - 0.0127mm shift (3.18 image voxels); green line - 0.0254mm (6.36 image voxels). The case

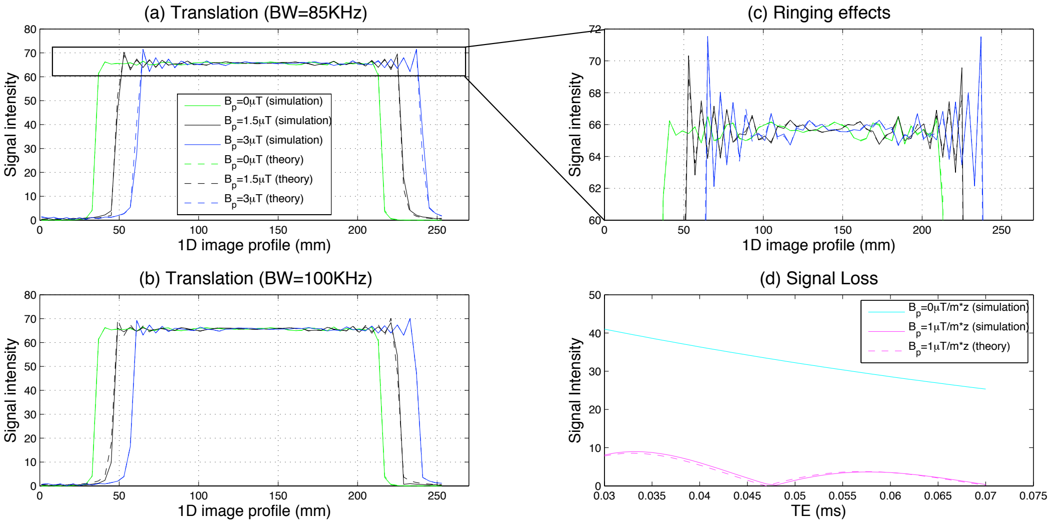

Figure 5.5: Figure shows effects of the $B_0$ field inhomogeneities: translation in the phase-encode direction ((a), (b) and (c)) and signal loss (d). Plots in (a), (b) represent 1D profiles (along the phase-encode direction) of the simulated 2D images representing one slice of the ellipsoid-shaped object. The plots also show Gibbs ringing effects due to the finiteness of the Fourier series in the process of image reconstruction (this can be more clearly seen in plot (c) which is an enlarged inset of plot (a)). Dashed lines in plots (a), (b) and (c) are 1D profiles (along the phase-encode direction) of 2D images that are the theoretical ('ideal') solutions which we obtained by analytically calculating the k-spaces (described in the text) and they show very close agreement with the simulated results. In some of the cases the difference between the theory and the simulations cannot be seen. Plot (d) is generated for a magnetic field with a linearly increasing inhomogeneity in direction of the positive z-axis $B_p = (\mu T/m) * z$ (full magenta line) while the light blue line shows the signal intensity for a magnetic field with no inhomogeneity. The dashed magenta line represents the analytically calculated signal loss using Eq. [5.3].

which shows the smallest amount of ringing (blue line) is due to an accidental, perfect alignment of the input object and the sampling matrix which happens very rarely in practice. No apodization of the k-space data was included in the image reconstruction. The capability to model ringing artefact demonstrates the usefulness of k-space-based simulations as it can not be generated with image-space-based simulations.

In order to show the amount of signal loss, the signal intensity is plotted (Figure 5.5) (d) for varying TE values in the case when there is no perturbed magnetic field (light blue line on the right hand plot), and in the case when the perturbed field linearly increases in the z-direction with a slope of $1\mu T/m$ (solid magenta line). Due to its dependence on TE, the dependence of the signal intensity in the distorted image is in the form of sinc function, which agrees with the theoretical results presented in Eq. [5.3] (magenta, dashed line).

## 5.3 Quantitative comparison of the simulation results with the real scan images

This section presents the work done on the experimental validation of the simulator. Experiments were devised for two different kinds of motion: translation along the z-axis and rotation about the x-axis. These two kinds were chosen as representatives because they respectively cover some of the most difficult motion effects to correct: spin history effects and interaction of the $B_0$ field inhomogeneities and motion.

Each of the experiments consisted of four steps:

1. Acquiring the images in the scanner
2. Running the simulator using the input values estimated from the scanned images
3. Analysing the scanner-acquired and the simulator-acquired data
4. Comparing the results of the simulator to the experimental results.

### 5.3.1 Translation in z

This section focuses on work done in validating the performance of the simulator when an object is moving along the z-axis (in either the + or - direction). One of the most complex effects of this type of motion is the spin history effect and validating that effect was the primary consideration of this section.

### Scanning

In order to test the performance of the simulator one of the most important factors was the choice of the input object. For an ideal validation a human subject would be used. However it is almost impossible for a human subject to move in a controllable way. Also, more importantly, there is lots of physiological signal in humans masking other changes. Therefore a simpler object was used: a grapefruit, which has a very high water content making the signal strong, and also which has very long $T_1$ time ($T_1 = 2531$ms) making spin history effects larger and therefore easier to analyse. This object was attached to a long stiff rod which was placed on the main bed of the scanner. One end of the rod (the one with the attached object) was placed inside the scanner bore, while the other end of the rod was outside the scanner bore and was held by the experimenter. The rod could be manually moved alongside a measurement tape either into or out of the bore which corresponds to +z or -z direction respectively.

An Echo Planar Imaging (EPI) series of 30 object volumes (3D images of the object) was acquired. The pulse sequence parameters used for the experiments were: $TR = 3$s, $TE = 30$ms, a matrix size of $64 \times 64$, 25 slices, an image voxel size $4 \times 4 \times 4$mm and a flip angle of $90°$. During the first 20 volumes the object was motionless. During the 21st volume the object was moved into the bore by 5mm (corresponds to 5mm in +z direction). The remaining 10 volumes were again motionless.

In addition to the motion images, additional images of the object were obtained: a $T_1$- weighted structural image, a field-map image and 12 spin-echo images. These extra images were acquired in order for some of the simulator

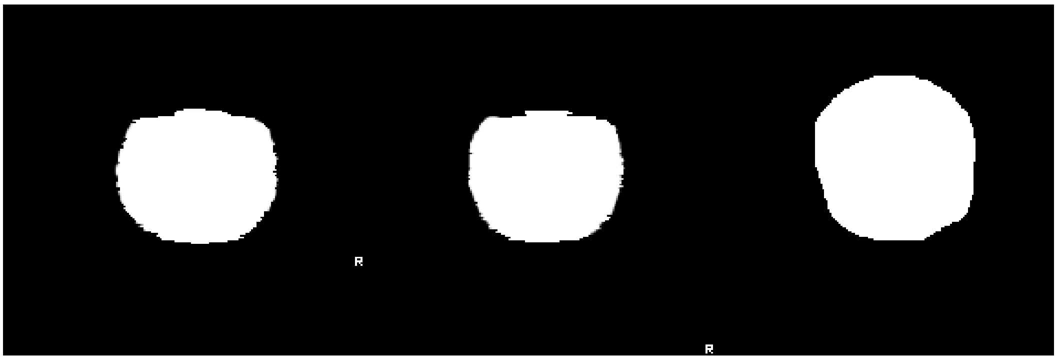

Figure 5.6: Mid-sagittal, -coronal and -axial slices of the input object (grapefruit) are showen from left to right. The size of the input object voxels were 1 × 1 × 1mm.

inputs to be extracted as described in the following section.

### Simulating

In order for the simulation to represent the real experiment as close as possible, each of the simulator inputs were derived from the experimentally obtained images of the grapefruit.

*Object:* In order to have the appropriate anatomical input into the simulator, a $T_1$-weighted structural image of the object is used. Due to the simplicity of the grapefruit, only one template (matter type) is extracted. The object used for the simulation is presented in Figure 5.6.

$B_0$ *perturbation field:* The amount of perturbation in the magnetic field is also estimated for each of the voxels. In Chapter 3 a description of the model for calculating $B_0$ inhomogeneities using known susceptibility values was given. Here a different approach was used. A field-map was firstly acquired (a couple of complex images scanned with different echo times). The field-map is then used to calculate the values of the perturbed field using FUGUE (FMRIB's Utility for Geometrically Unwarping EPIs [67]) . The perturbation images are shown in

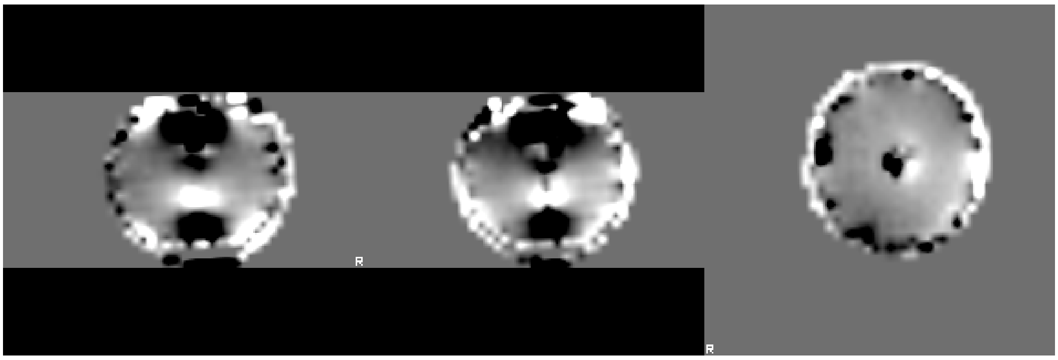

Figure 5.7: Mid-sagittal, -coronal and -axial slices of the pertubation field are shown from left to right. Magnetic field inhomogeneities evaluated for every voxel.

Figure 5.7.

*MR parameters:* The object was scanned using spin-echo acquisitions with different repetition times in order to measure $T_1$ and $T_2$ values [16]. The resulting values were obtained for each image voxel in the volume, which after averaging were: $T_1 = 2531$ms, $T_2 = 444$ms.

*Slice profile:* The Windowed-Sinc slice profile was estimated from a known RF waveform used for the scanning, and is shown in Figure 4.3.

*Pulse sequence:* The pulse sequence was generated in the pulse sequence generator of the simulator using the same parameters as the one used in the experiment (described above).

*Motion sequence:* The object was moved 5mm in +z direction during the acquisition of the 21st volume. However, the exact velocity and timing of motion, the precise times at which the motion began and ended within the 3s that took for the volume to be acquire, are not known. In order to learn more about the motion, the resulting images from the scanner were also examined. Several different options were tried, three of which are shown in Figure 5.8.

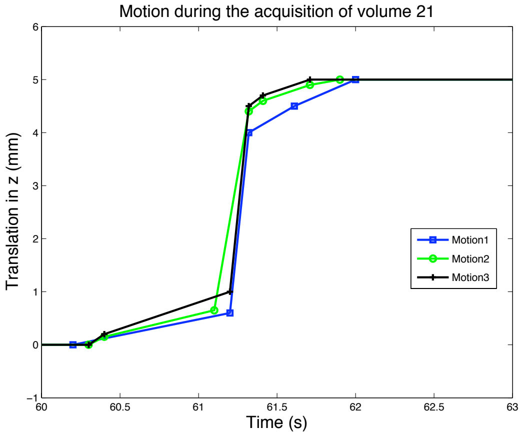

Figure 5.8: The object was moved 5mm during the acquisition of the 21st volume. The exact velocity and timing of this motion are unknown. Therefore, a number of different paradigms which could represent the motion that have occurred, are used in simulations.

## Analysing the data

In order to investigate how well the spin history effects were simulated spin history data was analysed in such a way as to emphasise only the spin history effect and not the predominant position displacement effect. The description of the analysis process is shown in Figure 5.9.

The top row represents the data set acquired either by real scanning or by simulation. The first 20 volumes were acquired while the object was motionless. During the acquisition of the 21st volume the object has moved to the new position in the scanner which is 5mm shifted in the +z direction from the initial position. The 22nd to 30th volumes were acquired while the object was motionless and situated in this new position. This is why in the figure these volumes appear slightly shifted compared with the initial volumes. The first four volumes of the data are erased to avoid the saturation effects (they usually occur in the first few volumes until the signal reaches the steady state).

The motion during the acquisition of the 21st volume was in the +z direction.

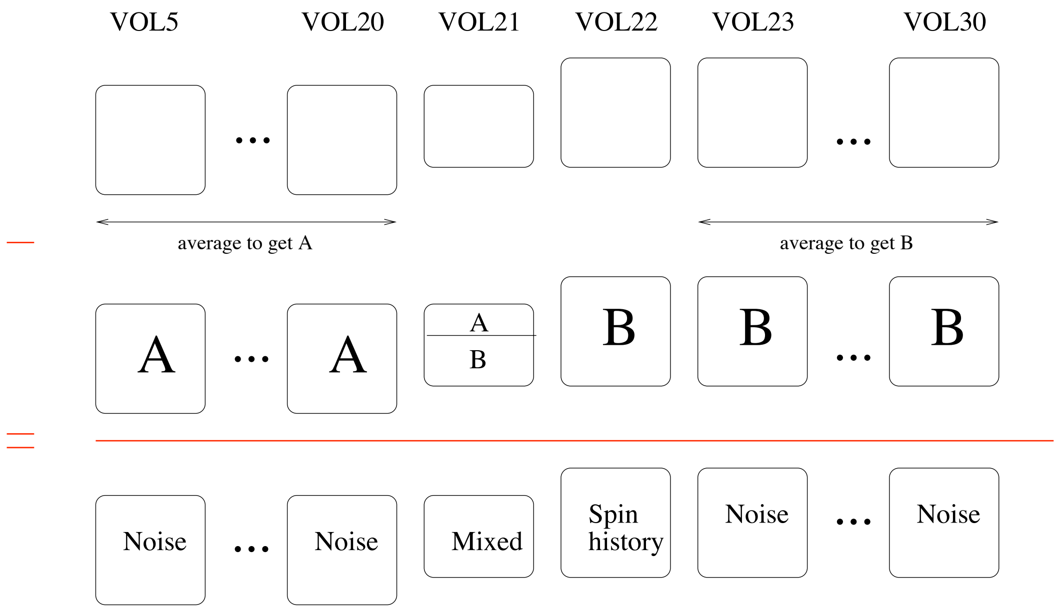

Figure 5.9: Descriptive representation of the analysis process. The bottom row is the first row minus the second row.

However, the slice selection order in this experiment ran in the -z direction. The motion and slice selections therefore took place at the same time but in opposite directions. As a result of this, some of the areas of the object were not scanned and the image of the 21st volume appears as if the bottom section has been lost (Figure 5.9) with mixed effects of position displacement, image distortion and spin history. However, the 22nd volume is affected only by the spin-history artefact. As a result of the movement the spins will "relax" shorter or longer than the fixed time-interval between the volumes (TR). The strongest impact in the signal is created by the spins which did not get excited during the 21st volume, and therefore will "relax" for 6s which is much longer than the fixed 3s time-interval.

In order to capture only the spin history effects, all of the other effects are subtracted from the data. This is done by averaging the first 16 volumes to obtain volume “A”, averaging the last 7 volumes to obtain volume “B” and then connecting all of them into the AB set. The 21st volume of the AB set is obtained by combining the A and B volumes as shown in Figure 5.9. The newly created AB set is subtracted from the data and the required spin history effects are found isolated in the 22nd volume.

Motion effects vary from voxel to voxel within each of the slices. In order to obtain a single value for each of the slices, each slice of the original data was masked to exclude the background values and then averaged. This is done before the analysis process described above.

### Results and Discussion

Firstly, the images obtained from the experiment are shown in Figure 5.10. The images acquired by the scanner are shown in the top row and the images acquired by the simulator are shown in the bottom row. Mid-sagittal, -coronal and -axial slices of volume 21 (from left to right) are shown. Motion occurred *during* the acquisition of volume 21. It can be seen that the experimental and the simulation results match well regarding the image distortions due to $B_0$ inhomogeneities.

The results of the analysis process which investigates the spin-history artefact are shown in Figure 5.11. This figure shows the percentage of the signal change due to the translation in +z direction. The motion happened during the acquisition of the 21st volume and the resulting effects for both the real and simulated data are shown on the left. The spin-history artefact is present in the 22nd volume and this is shown in the plot on the right hand side of the figure. It can be seen from the figure that within a very small range of motion paradigms, the range of spin-history effects can be seen that include the real one (red line). It can be seen also that the results are very sensitive to the particular the motion that occurred during the acquisition of the 21st volume. This is the most likely

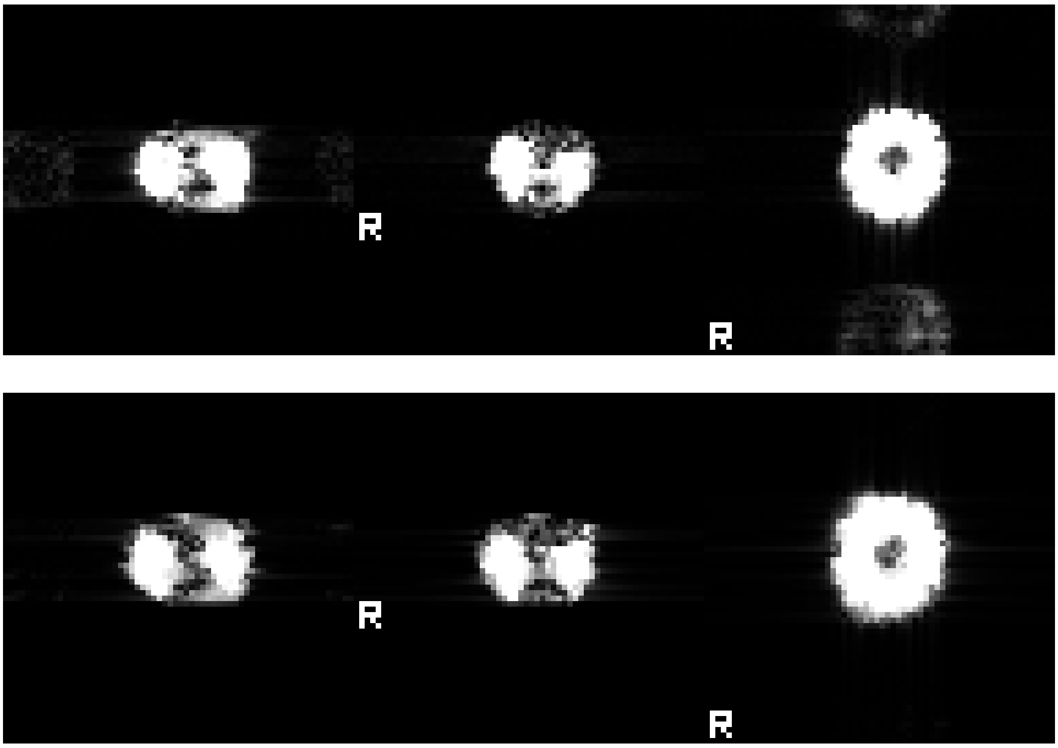

Figure 5.10: Experimental results (top), simulation results (bottom). Mid-sagittal, -coronal and -axial slices of volume 21 are shown (from left to right).

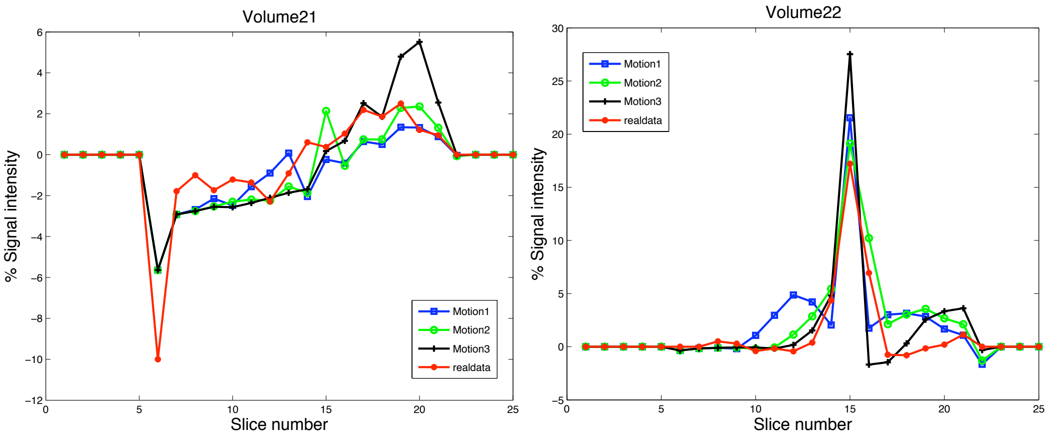

Figure 5.11: The percentage of the signal change due to the translation in +z direction is shown. The x-axis in the plots represents the z-axis of the object and is marked with the slice numbers. Progression from 1 to 25 slices is equivalent to progression in z+ direction in the scanner.

reason for their imperfect match. If it were possible to produce the exact type of motion as the one that happened during the real scanning process we could expect to see a closer match between the real and simulated data than the ones shown in Figure 5.11.

### 5.3.2 Rotation about the y-axis

This section focuses on work done in validating the performance of the simulator when an object is rotating about the y-axis. One of the most complex effects of this type of motion is the effect of interaction of $B_0$ inhomogeneities (due to susceptibility) and motion and validating that effect was the primary consideration of this section.

**Scanning**

As in the case of translation described in the previous section, a simple object was used for the experiments. This object was a glass sphere filled with gelatin. In addition to gelatin, an extra structure built of wood and a plastic air bubble was inserted into the sphere with a goal of creating susceptibility-induced $B_0$ inhomogeneity artefacts. The object was attached to a long stiff rod which was placed on the main bed of the scanner. One end of the rod (the one with the attached object) was placed inside the scanner bore, while the other end of the rod was outside the scanner bore and was held by the experimenter. The rod could be manually moved alongside a measurement tape either left or right which corresponds to rotation about y-axis of the scanner.

An Echo Planar Imaging (EPI) series of 30 object volumes (3D images of the object) was acquired. The pulse sequence parameters used for the experiments were: $TR = 3\text{s}$, $TE = 30\text{ms}$, a matrix size of $64 \times 64$, 36 slices (with the slice acquisition order that ran in -z direction), an image voxel size $4 \times 4 \times 4$mm and a flip angle of 90°. During the first 19 volumes the object was motionless. During the 20th volume the object was rotated by 15 degrees about y-axis. The remaining 11 volumes were again motionless.

In addition to the motion images, additional images of the object were obtained: a $T_1$-weighted structural image, a field-map image and 12 spin-echo images. These extra images were acquired in order for some of the simulator inputs to be extracted as described in the following section.

### Simulating

In order for the simulation to represent the real experiment as close as possible, each of the simulator inputs were derived from the experimentally obtained images of the sphere.

*Object:* In order to have the appropriate anatomical input into the simulator, a $T_1$-weighted structural image of the object is used. The object used for the simulation is presented in Figure 5.12. The wooden part inside the object was assumed not to give any signal (as it has considerably less water molecules than the rest of the object) and was given a spin density of zero.

*$B_0$ perturbation field:* As described in Chapter 4, Section 2 a set of precomputed basis functions is needed as an input to the simulator. In order to do this, a perturbation method for solving Maxwell's equations was used [37] (as described in more detail in Chapter 3, Section 3). Two different basis sets were generated, one for the sphere with gelatin and the other for the wooden stick inside the sphere. These two basis sets were then linearly combined in order to form a final basis set for the whole object. In order to calculate the correct coefficients in the linear model of the two basis sets, the appropriate pair was fitted to the experimentally derived perturbed field. This perturbed field was

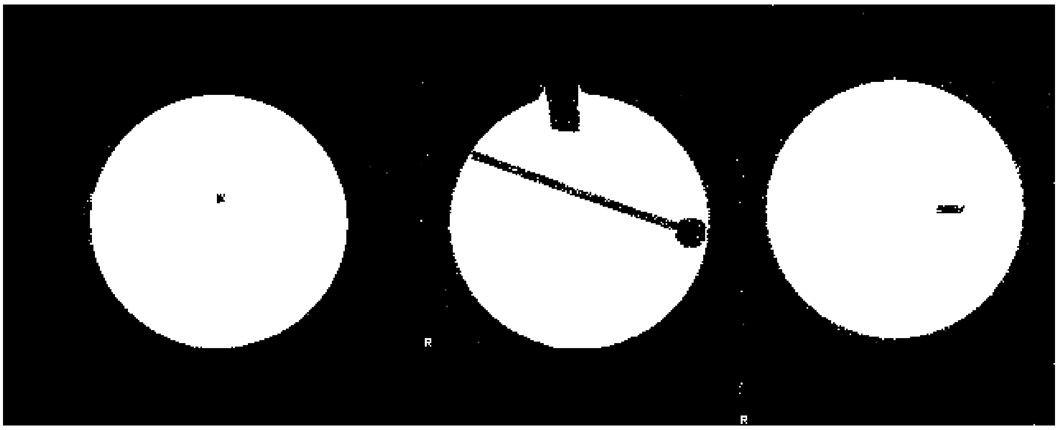

Figure 5.12: The input object. The size of the input object voxels were 1 × 1 × 1mm.

calculated from a field-map acquired during the scanning (using PRELUDE and FUGUE [67]). An example vector of the final basis set is shown in Figure 5.13.

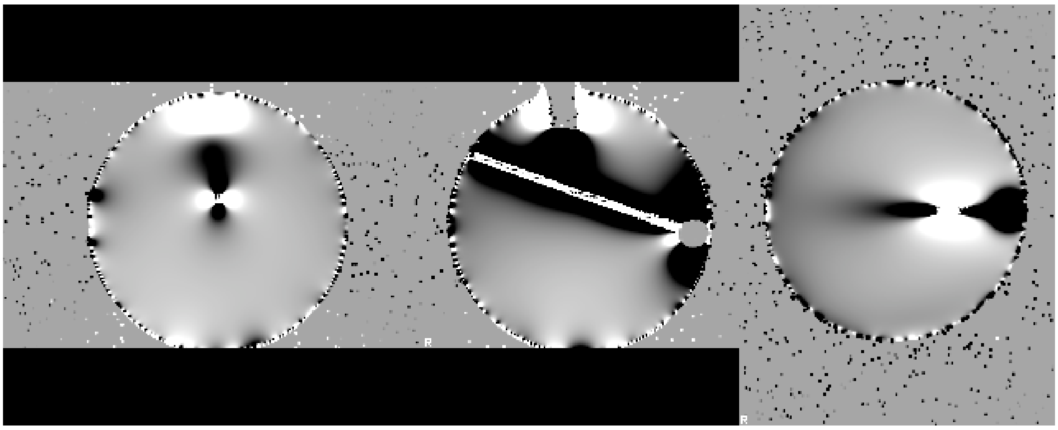

Figure 5.13: An example basis vector of the basis set of the $B_0$ perturbation field.

*MR parameters:* The object was scanned using spin-echo acquisitions with different repetition times in order to measure $T_1$ and $T_2$ values [16]. The resulting values were obtained for each image voxel in the volume, which after averaging were: $T_1 = 1125$ms, $T_2 = 100$ms.

*Slice profile:* The Windowed-Sinc slice profile was estimated from a known RF waveform used for the scanning, and is shown in Figure 4.3.

*Pulse sequence:* The pulse sequence was generated in the pulse sequence generator of the simulator using the same parameters as the ones used in the experiment (described above).

*Motion sequence:* The object was rotated by 15 degrees about the y-axis during the acquisition of the 20th volume. However, as in the case of translation which was described in the previous section, the exact velocity and timing of motion are not known. In order to learn more about the motion, the resulting images from the scanner were examined to determine the timing by subjective assessment. The resulting motion paradigm was used in the simulations and is shown in Figure 5.14.

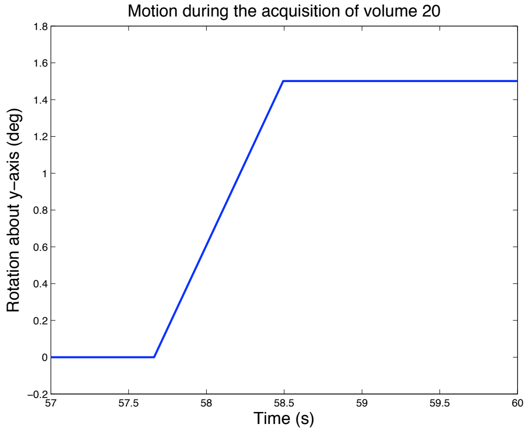

Figure 5.14: The object was rotated by 15 degrees about the y-axis and during the acquisition of the 20th volume. The exact velocity and timing of motion were not known and therefore in order to choose the correct motion paradigm, the resulting images from the scanner were also examined.

### Analysing the data

In order to investigate how well the motion interaction with the $B_0$ inhomogeneities was simulated, data was analysed in such a way as to emphasise only this effect. Firstly part of the analysis was done in the same way as for the previous experiment (Translation in z).

The first four volumes of the data are erased to avoid the saturation effects (they usually occur in the first few volumes until the signal reaches the steady state). The following 16 volumes are averaged to obtain volume "A". The motion happened during the acquisition of volume 20, and this volume (and a subsequent one) will therefore contain mixed effects of spin history artefact, and the interaction between the motion and the $B_0$ inhomogeneities. In order to avoid both of the effects, these couple of images are also erased from the data and the following 8 are averaged to obtain volume "B". The averaged volumes are then subtracted from the original data set. The resulting data set (specifically volume 20) should contain just the spin-history artefact and the interaction between the motion and the $B_0$ inhomogeneities. More details about this analysis can be found in the previous section (see Figure 5.9).

The second part of the analysis was done in order to investigate how well the change in $B_0$ inhomogeneities due to motion was simulated. In order to do this averaged volumes before ("A") and after ("B") the motion took place were compared. Volumes "A" and "B" (which were explained in the previous paragraph) are motion corrected in order to match. A plane that contains the wooden stick (inside the object) and is parallel to y-axis, was extracted from both of the images. The plane from volume "A" was then subtracted from the plane from volume "B". The differences between the two planes (the area underneath the wooden stick) should be only due to the voxels experiencing different amounts of $B_0$ inhomogeneities. The direction of the translation in y-direction (phase-encode direction) due to the $B_0$ inhomogeneities should remain the same between the two. This is because the motion was purely rotation about the y-axis and therefore the two planes remain parallel to the y-axis before and after the motion happened. In addition to these results, a set of data was also simulated without the $B_0$ inhomogeneities. The same kind of analysis as the one described earlier was applied to this data set.

### Results and Discussion

Firstly, the images obtained from the experiment are shown in Figure 5.10. The images acquired by the scanner are shown on the left hand side and the images acquired by the simulator are shown on the right hand side. Mid-sagittal, -coronal and -axial slices of volumes 19, 20 and 21 (from top to bottom) are shown. Motion occurred *during* volume 20 and this can be seen in the images by looking at the wooden stick (which acts as a useful reference point) which is considerably bent in this volume. It can also be seen that the position of the wooden stick is different in volumes 19 and 21 reflecting the time points just before and after the motion took place. It can also be seen that the experimental and the simulation results match well both regarding the gross motion effects and the effect $B_0$ inhomogeneities.

Results of the first part of the analysis are shown in Figure 5.16. Mid-sagittal, -coronal and -axial slices of volume 20 are shown for both the experimental (top) and simulated (bottom) data. Both sets of data were analysed in the same way which is described in the Methods section. Volume 20 should only contain the interaction between the motion and $B_0$ inhomogeneities (together with some effect of the spin history). The patterns in the simulated and the experimental data showed a good level of agreement, specifically in the areas around the wooden stick where the largest interactions between the motion and the $B_0$ inhomogeneities

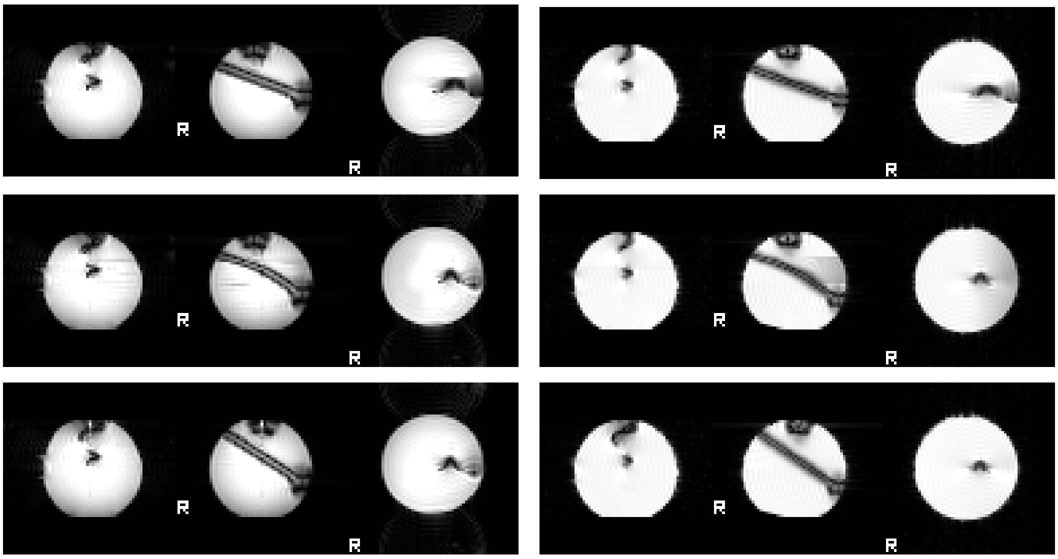

Figure 5.15: Experimental results (left), simulation results (right). Mid-sagittal, -coronal and -axial slices of volumes 19, 20, and 21 (from top to bottom). Motion occurred during the acquisition of volume 20 and this can be seen by the look of the bent wooden stick inside the object.

are expected due to the susceptibility differences between the stick and the surrounding gelatin. These can be seen mainly in the middle and the right hand images.

The results of the second part of the analysis process are shown in Figures 5.17 and 5.18. Figure 5.17 shows the plane from volume “A” containing the wooden stick and is parallel to the y-axis (left), the plane from volume “B” containing the wooden stick and is parallel to the y-axis (middle) and the subtraction of the planes (right). The experimental results are shown in the top row, the simulation results which were generated with the presence of $B_0$ inhomogeneities are shown in the middle row, and the simulation results which were generated without the presence of $B_0$ inhomogeneities are shown in the bottom row.

The two top rows in the figure agree well in the way $B_0$ inhomogeneities affected the images before and after the motion occurred. This can be more clearly

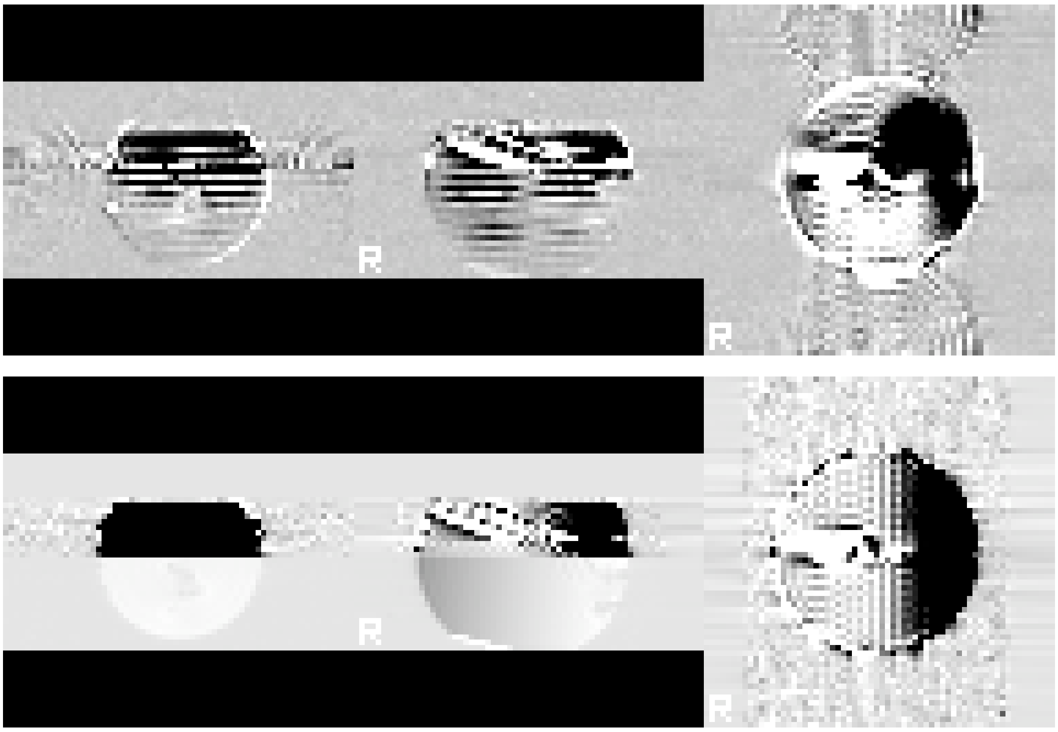

Figure 5.16: Intensity patterns in the motion-affected volume 20 are shown for both the experimental (top) and simulated (bottom) analysed data. The images contain the effects of interaction of the motion and $B_0$ inhomogeneities, (though some spin-history effects are also present).

seen in the difference images on the right hand side of the figure which are showing the difference in the image intensity due to $B_0$ inhomogeneity-based distortion which was changing with the positional displacement of the object. On the other hand, the difference image on the bottom, generated as if there is no $B_0$ inhomogeneity, shows that the position displacement did not greatly affect the intensity of the images. In order to see these results more clearly, an averaged 1D profile of the images in Figure 5.17 is shown in Figure 5.18. It can be seen in Figure 5.18 how 1D profiles of the experimental and the simulated data (with $B_0$ inhomogeneities) match well. The simulated data generated without $B_0$ inhomogeneities confirms that the change in the profiles is due to $B_0$ inhomogeneities.

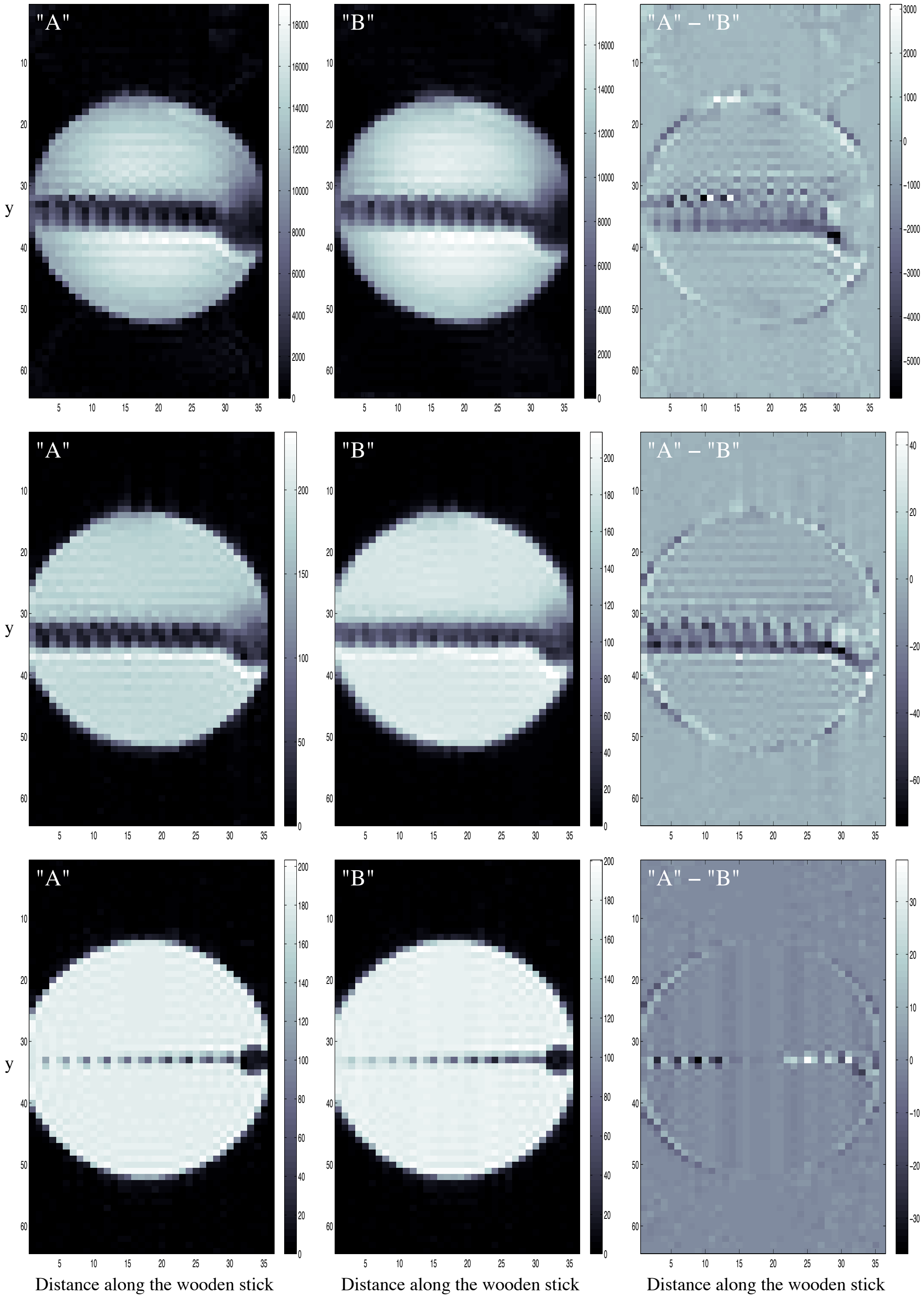

Figure 5.17: The plane from volume "A" containing the wooden stick and is parallel to the y-axis (left), the plane from volume "B" containing the wooden stick and is parallel to the y-axis (middle) and the subtraction of the planes (right). Note that the vertical axis in this figure is the y-axis, and the horizontal axis is the axis along the wooden stick (both in voxels). The experimental results (top), the simulation results with $B_0$ inhomogeneities (middle), and the simulation results without the presence of $B_0$ inhomogeneities (bottom).

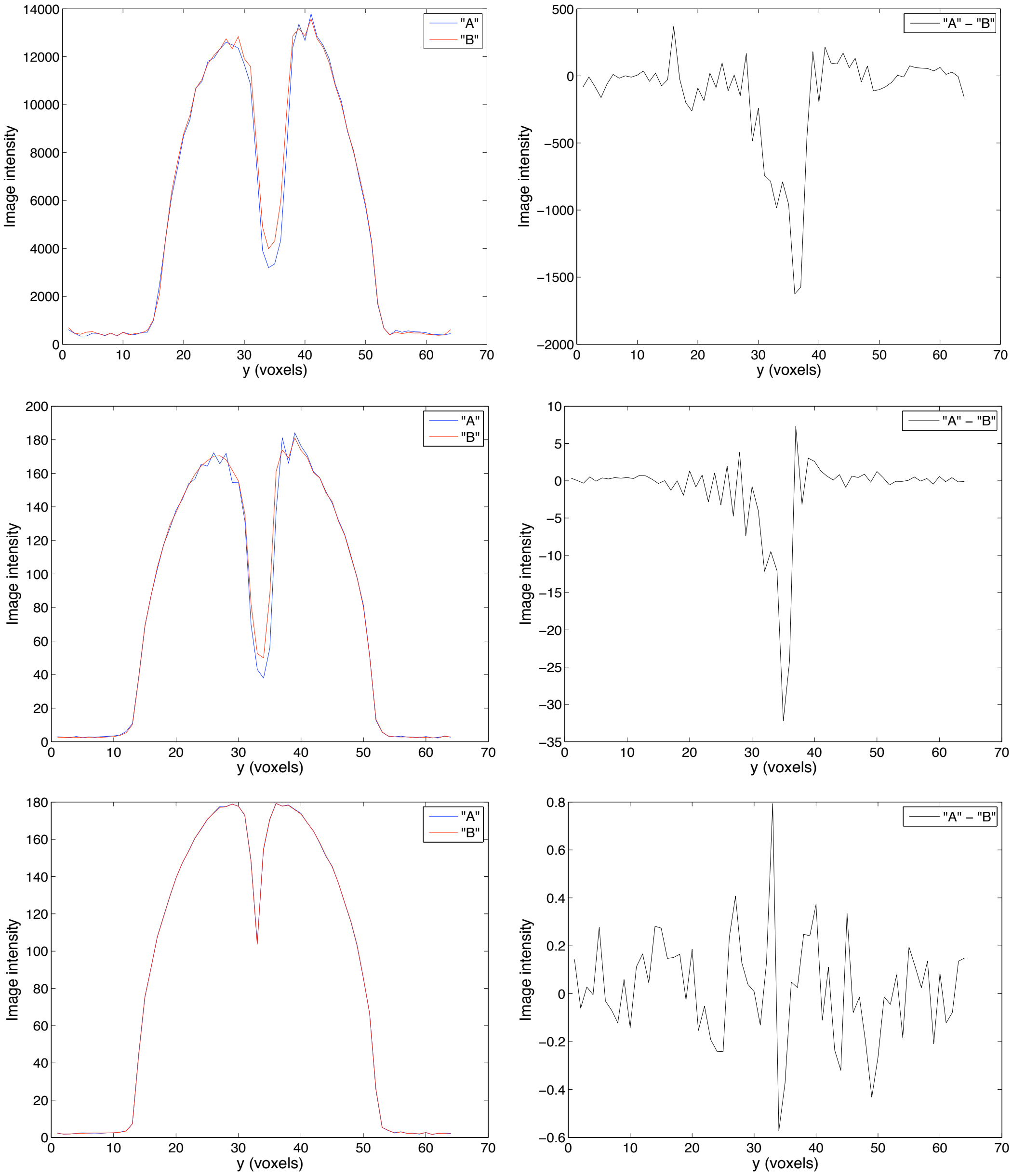

Figure 5.18: Averaged 1D profiles of "A" (the blue line on the left) and "B" (the red line on the left) images shown in Figure 5.17 and their subtraction "A" - "B" (the black line on the right). The averaging took place along the direction of the wooden stick. The experimental data are shown in the top row, the simulated data (with $B_0$ inhomogeneities) are shown in the middle row, and the simulated data (without $B_0$ inhomogeneities) are shown in the bottom row.

## 5.4 Qualitative comparison of the simulation results with real scan images

In this section a small selection of examples of simulated datasets are shown which are using a realistic brain phantom as an object. Most of these examples of these examples are qualitative in nature, (with an exception of the chemical shift simulation) and we present them in order to illustrate the similarity between the simulated and real images. Artifacts presented in this section are: ghosting, chemical shift, $B_0$ inhomogeneity, eddy currents and within-scan motion.

In all of the examples we used the McGill virtual brain [19] with the parameter values given in Table 4.1, at 3T magnetic field strength, and an EPI pulse sequence which we generated with parameters: TE = 30ms, TR = 3s, flip angle 90°, maximum gradient strength 35mT/m, rise time 0.2ms, and crushers of maximum magnitude. It is important to note that even very small mistakes in generating the pulse sequence cause various artefacts in the simulated images, as is the case with a real scanner. An example of this is ghosting (Figure 5.19) that we obtained

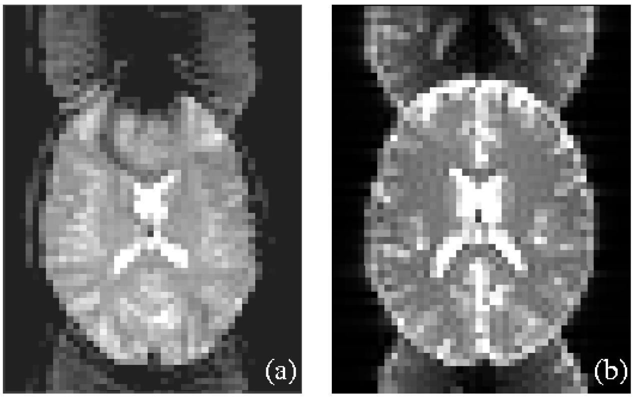

Figure 5.19: Figures show ghosting due to a user-gradient mis-specification both in a real image (a) and a simulated image (b). The additional distortion in the frontal area of the brain in the real image is due to the susceptibility effect which was not included in this simulation. The resolution in the cross-sectional plane in both images is 4 × 4mm.

by using a pulse sequence with a very small (less than one millisecond) delay in the echo timing.

Chemical shift artefact is shown in Figure 5.20. The figure is generated using grey, white, CSF and fat tissues and represents the effect of difference in the chemical shift between fat and other tissues in the brain. It also shows the

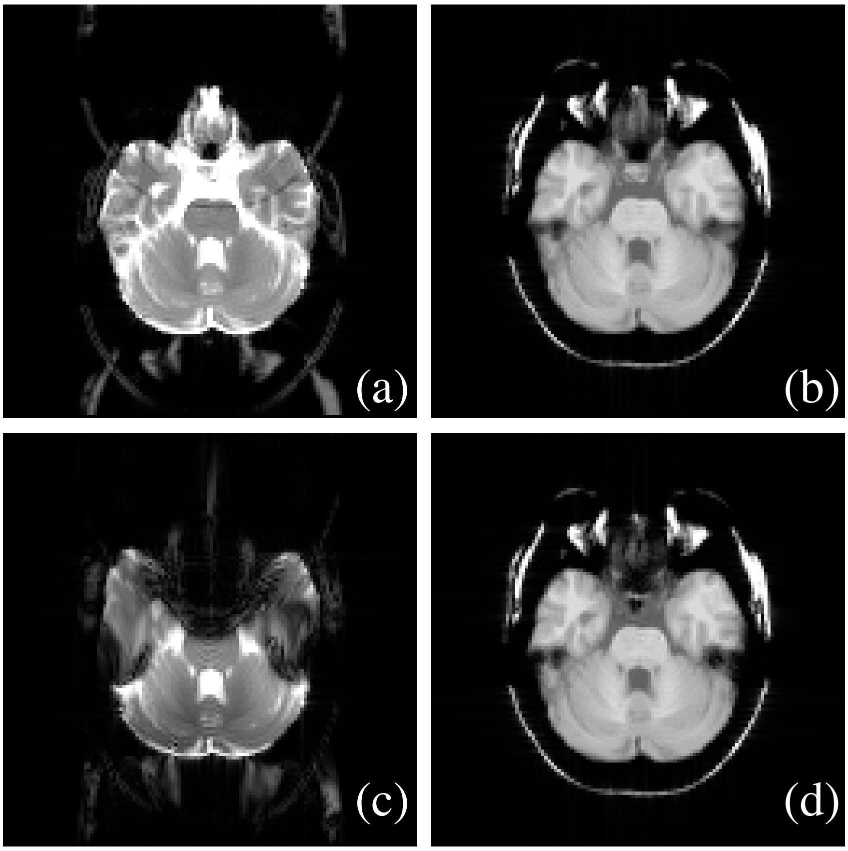

Figure 5.20: Figures showing the effect of chemical shift at 3T in (a) an EPI image without $B_0$ inhomogeneities; (b) $T_1$-weighted standard gradient echo image without $B_0$ inhomogeneities; (c) an EPI image with $B_0$ inhomogeneities; and (d) $T_1$-weighted standard gradient echo image with $B_0$ inhomogeneities. All images are simulated with a resolution in the cross-sectional plane of $2 \times 2$mm. The shift of the fat tissue due to the chemical shift is: (a) and (c) 178mm in phase encode direction (along negative $y$-axis) which at this resolution is 79 image voxels; (b) and (d) 1.1mm in the frequency encode direction (along positive $x$-axis) which at this resolution is 0.55 image voxels. These shifts were calculated from the theory and they match closely with the simulations. It can also be seen in the figure how the effects of the artefacts are much stronger in the EPI image than in the standard gradient echo image.

different intensity and characteristics of the chemical shift artefact in two different pulse sequences: an EPI imaging sequence (resolution 2 × 2mm, TE = 30ms, TR = 3s) and a $T_1$-weighted standard gradient-echo imaging sequence (resolution 2 × 2mm, TE = 8ms, TR = 300ms). Both imaging sequences used 90° flip angle, maximum gradient strength 35mT/m, rise time 0.2ms, and crushers of maximum magnitude. Simulations were generated without $B_0$ inhomogeneities as shown in Figures 5.20 (a) and (b), and with $B_0$ inhomogeneities in Figures 5.20 (c) and (d). Chemical shift values that were used are shown in Table 4.1.

The expected amount and the direction of the resulting shift of the fat tissue in the output images that is due to the chemical shift differences is analytically calculated for both sequences using Eq. [5.3] (EPI sequence) and equation $\triangle x = \delta B_0/G$ [48] where $\triangle x$ is the amount of the translation in the x direction, $\delta$ is the shielding constant and $G$ is the frequency encoding gradient (standard gradient echo sequence). For the EPI sequence it is estimated to be 178mm (out of 256mm in total) in the phase encode direction (along the $y$ axis) and that is seen in Figures 5.20 (a) and (c); and for the standard gradient echo sequence, it is 1.1mm (out of 256mm in total) in the frequency encode direction (along the $x$-axis) which is shown in Figures 5.20 (b) and (d) but is so small that can not be seen simply by eye. In Figures 5.20 (a) and (c) we can also see some effects of ghosting of the fat signal which is also part of the chemical shift artefact.

Figure 5.21 represents the effect of $B_0$ field distortions in the simulation, shown in (b), versus the case with no $B_0$ field distortions, shown in (a). We used an EPI pulse sequence and a resolution of 4 × 4 × 6mm in this simulation. As expected, the biggest distortions and signal loss we obtained were in the areas close to the air pockets in the skull, which look very similar to a real scanning case shown in (c).

We also simulated the effects of the eddy currents. An example of the simula-

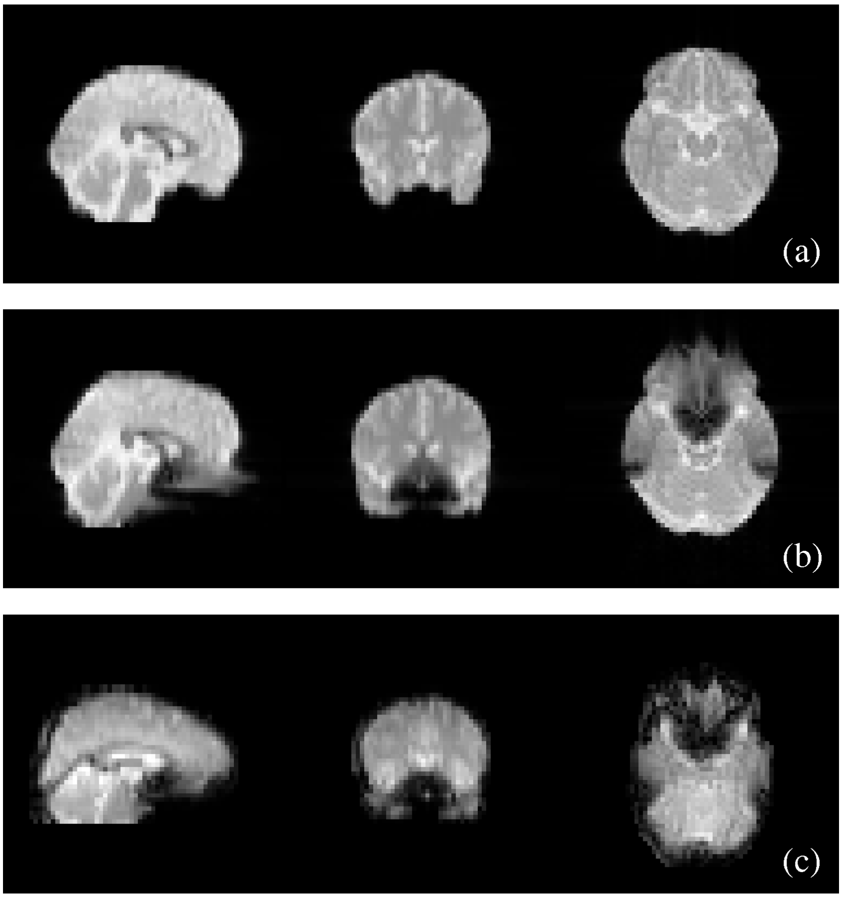

Figure 5.21: An example of an EPI scan of sagittal, coronal and axial slices generated at 3T magnetic field and with resolution $4 \times 4 \times 6$mm, TE = 30ms, flip angle 90°, maximum gradient strength 35mT/m and rise time 0.2ms, matrix size $64 \times 64$ where (a) is a simulated scan with no artefacts, (b) is a simulated scan with $B_0$ field distortion and (c) is a real scan (different subject) with $B_0$ field distortions. Note how similar the real (c) and the simulated (b) distortions look like, specially distortions in the frontal lobe and around the ears.

tion is presented in Figure 5.22 with a resolution of $2 \times 2$mm in the cross-sectional plane. The eddy currents in this example were generated by gradients applied in the read-out direction before the actual signal acquisition took place. More details about the simulation of eddy currents are given in Chapter 6.

Blurring due to the object's movement during the read-out period was also simulated. Figure 5.23 shows the effects of a rigid-body rotation about the $z$-axis

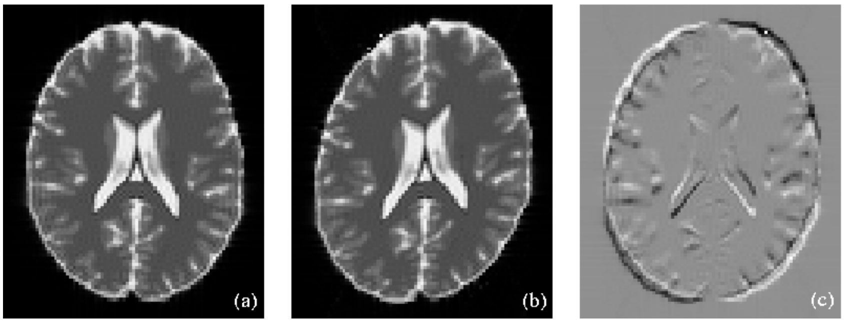

Figure 5.22: Example images showing the effects of eddy currents on an EPI image: (a) $T_2$-weighted image; (b) $T_2$-weighted image with eddy currents; (c) Subtraction of image (a) from image (b). All images have a resolution of 2 × 2mm in plane and TE = 30ms.

that happened during the signal acquisition time i.e. during the read-out period. Note that the motion is exaggerated here (9 degrees) to make the artefact clearly visible although much smaller movements still induce artefacts which, although not easily visible to the eye, are potentially large enough to significantly impact the FMRI statistics.

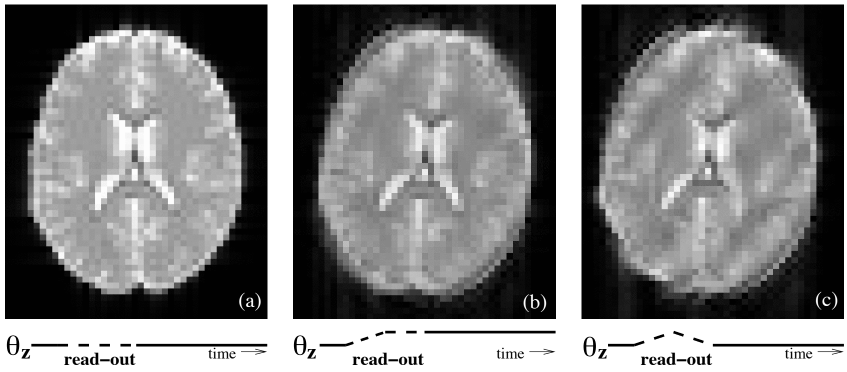

Figure 5.23: Example images showing the effects of within-scan motion (rigid-body rotation about the $z$-axis) on an EPI image: (a) no motion; (b) constant rotation; (c) back and forth rotation. Note that the degree of motion is exaggerated here (9 degrees) to illustrate the effect visually. The line underneath the image represents the angle of rotation as a function of time with the read-out portion of the sequence represented with a dashed line.

## 5.5 Summary

This chapter described the steps taken in order to validate the simulator. The sensitivity of the simulator regarding the object voxel size was investigated. The magnetic-susceptibility-induced $B_0$ inhomogeneity model was validated. The simulated results, the amount of translation in phase encode direction, and the amount of signal loss, showed excellent agreement with the known theoretical results. The motion model was validated experimentally using simple objects for which MR relaxation times were measured and field maps were calculated. The scanner-acquired data showed very good agreement with simulator-acquired data for all of the cases of motion. Chemical shift results were generated for a realistic brain phantom. The translation observed in the fat tissue due to the chemical shift agreed excellently with the shift calculated using the theoretical equations.

So far in this thesis the whole process of the development of the simulator has been described: the simulation model, the implementation of that model and the validation of the simulator. The next chapter describes the applications of the simulator, demonstrating its usefulness in various aspects of MRI-related research.